Nuclear Science and Techniques (2025) 36:170
https://doi.org/10.1007/s41365-025-01761-w

Constraining the chiral magnetic effect using spectator and participant planes across Au+Au and isobar collisions at $\sqrt{s_{\rm NN}} = 200$ GeV

Bang-Xiang Chen[1] · **Xin-Li Zhao**[2,3] · **Guo-Liang Ma**[1,2]

Received: 14 January 2025 / Revised: 25 February 2025 / Accepted: 13 March 2025 / Published online: 29 June 2025

Abstract
We investigated the chiral magnetic effect (CME) in relativistic heavy-ion collisions through an improved two-plane method analysis of the $\Delta\gamma$ observable, probing $\mathcal{CP}$-symmetry breaking in the strong interactions and topological properties of the QCD vacuum. Using a multiphase transport model with tunable CME strengths, we systematically compared the Au+Au and isobar collisions at $\sqrt{s_{\rm NN}} = 200$ GeV. We observed a reduced difference in the CME signal-to-background ratio between the spectator and participant planes for Au+Au collisions compared with isobar collisions. A comprehensive chi-square analysis across all three collision systems revealed stronger CME signatures in Au+Au collisions than in isobar collisions, particularly when measured with respect to the spectator plane. Our findings demonstrate the enhanced experimental reliability of the two-plane method for CME detection in Au+Au collisions.

Keywords Chiral magnetic effect · Relativistic heavy-ion collisions · Quark–gluon plasma · Magnetic field

1 Introduction

Relativistic heavy-ion collisions create a unique environment where a quark–gluon plasma with strong collectivity is formed [1–8], accompanied by the strongest known magnetic field generated by spectator protons from the colliding nuclei [9–16]. This environment provides an ideal laboratory for studying the topological properties of the QCD vacuum and anomalous chiral transport phenomena under extreme magnetic field conditions. The chiral magnetic effect (CME), which induces electric charge separation along the magnetic field direction in systems with chiral imbalances, is crucial for detecting these phenomena [17–19].

The charge-dependent azimuthal correlation $\gamma_{\alpha\beta} = \langle\cos(\phi_\alpha + \phi_\beta - 2\Psi_{\rm RP})\rangle$ was initially proposed as a potential observable for detecting the CME [20]. In this correlator, $\phi_{\alpha(\beta)}$ denotes the azimuthal angle of a charged particle $\alpha(\beta)$, and $\Psi_{\rm RP}$ represents the angle of the reaction plane. The difference between opposite-charge and same-charge correlations is represented by $\Delta\gamma$. Early measurements of this correlation by the STAR Collaboration [21–24] at RHIC and the ALICE Collaboration [25] at the LHC aligned with CME expectations. However, significant background effects, especially those arising from an elliptical flow, influence the measured correlator [26–31]. In recent RHIC–STAR measurements [32], the best measurement was 14.7% in 20–50% centrality for the full-event method, although there could be residual non-flow background as well as discrepancy between a and b. Some measurements incorporating the non-flow effect have limited the CME

This work was supported by the National Key Research and Development Program of China (No. 2022YFA1604900), the National Natural Science Foundation of China (Nos. 12147101, 12325507, and 12105054), and the Guangdong Major Project of Basic and Applied Basic Research (No. 2020B0301030008).

✉ Guo-Liang Ma
glma@fudan.edu.cn

Xin-Li Zhao
zhaoxinli@usst.edu.cn

[1] Key Laboratory of Nuclear Physics and Ion-beam Application (MOE), Institute of Modern Physics, Fudan University, Shanghai 200433, China

[2] Shanghai Research Center for Theoretical Nuclear Physics, NSFC and Fudan University, Shanghai 200438, China

[3] College of Science, University of Shanghai for Science and Technology, Shanghai 200093, China

fraction to approximately 10% [33–37] for Au+Au collisions at $\sqrt{s_{\rm NN}} = 200$ GeV. Several methods have been proposed for separating potential CME signals from the dominant background [34, 36, 38–41]. One promising approach involves using isobar collisions, which consist of systems with the same nucleon number but different proton numbers, such as ${}^{96}_{44}$Ru +${}^{96}_{44}$ Ru and ${}^{96}_{40}$Zr +${}^{96}_{40}$ Zr collisions [42, 43]. The latest STAR evaluation of the CME signal established an upper limit of approximately 10% for the CME fraction in the $\Delta\gamma$ measurement at a 95% confidence level in isobar collisions at $\sqrt{s_{\rm NN}} = 200$ GeV, after correcting for non-flow contamination [44–46]. However, the nuclear structure effect poses a challenge when searching for the CME in isobar collisions because it introduces differences in the backgrounds of the two isobar systems [47–57]. Based on the AMPT model, the newly developed state-of-the-art Chiral Anomalous Transmission (CAT) module reveals that the upper limit of the CME signal in isobar collisions is 15% [58, 59], which aligns with the STAR data.

Numerous experimental observables have been employed to detect true CME signals while minimizing the background interference in Au+Au and isobar collisions. For this purpose, a two-plane measurement method utilizing charge-dependent azimuthal correlations relative to the spectator plane (SP) and participant plane (PP) was proposed [60, 61]. This method is based on the fact that background and CME signals exhibit different sensitivities or correlations to the two planes [62]. The STAR collaboration applied this method to quantify the fraction of the CME signal within the inclusive $\Delta\gamma$ correlation in both Au+Au and isobar collisions. For Au+Au collisions at $\sqrt{s_{\rm NN}} = 200$ GeV, the STAR results suggest that the fraction of CME-induced charge separation is consistent with zero in the peripheral centrality bins, whereas finite CME signals may exist in the mid-central centrality bins [32]. This method is believed to eliminate most of the collective flow effect in the background; however, certain non-flow background effects require further investigation [37]. Furthermore, the SP and PP methodology assumes that the ratio a of the elliptical flow relative to different reaction planes is equivalent to the ratio b of the CME signals relative to different reaction planes [32, 37, 63]. However, these two ratios may differ. In our previous study [64], we calculated the CME signal-to-background ratio of b over a ($b/a = 0.65 \pm 0.18$) in isobar collisions at $\sqrt{s_{\rm NN}} = 200$ GeV using the AMPT model with an initial CME signal, thereby providing theoretical support for the experimental measurement of the CME in isobar collisions. In this study, the experimental search for CME signals in Au+Au collisions and the need to explore the values of b across different collision systems motivated us to extend our calculations to Au+Au collisions at $\sqrt{s_{\rm NN}} = 200$ GeV. We aimed to simultaneously fit the experimental observables related to the CME in three different collision systems, Au+Au, Zr+Zr, and Ru+Ru, within the AMPT model framework, thereby achieving a synchronous constraint and extraction of the CME strengths in these three collision systems. We focus on studying how the evolution of different collision systems affects the imported CME signal, which is introduced manually rather than derived from first principles, such as the magnetic field and chirality imbalance.

The remainder of this paper is organized as follows. In Sect. 2, we describe the setup of the AMPT model with an initial CME signal and outline our two-plane method for extracting the fraction of the CME signal from the inclusive $\Delta\gamma$. Our model results are presented and compared with measurements from the STAR experiment in Sect. 3, in which we discuss the implications of our findings for the interpretation of the experimental data and possible physical sources. Finally, Sect. 4 summarizes the main conclusions of the study.

2 Model and method

2.1 The AMPT model with initial CME signal

The AMPT model is a multiphase transport framework designed to simulate the four main stages of relativistic heavy-ion collisions [65–67], which includes the following components:

(1) The HIJING model provides the initial conditions. The transverse density profile of the colliding nucleus is modeled as a Woods–Saxon distribution. Multiple scatterings among the participant nucleons generate the spatial and momentum distributions of minijet partons and soft excited strings. Using a string-melting mechanism, quark plasma is generated by melting the parent hadrons.
(2) Zhang's parton cascade (ZPC) model simulates the parton cascade stage. The ZPC model describes parton interactions via two-body elastic scattering. The parton cross section is calculated using leading-order pQCD for gluon–gluon interactions.
(3) A quark coalescence model combines two or three nearest quarks into hadrons to simulate hadronization.
(4) A relativistic transport (ART) model simulates the stage of hadronic rescatterings, including resonance decays and all hadronic reactions involving elastic and inelastic scatterings among baryon–baryon, baryon–meson, and meson–meson interactions.

Numerous previous studies have demonstrated that the AMPT model effectively describes various experimental observables

in both large and small collision systems at the RHIC and LHC [65–74].

According to the methodology described in Ref. [75], we implemented a CME-like charge separation mechanism in the initial partonic stage of the AMPT model. The CME signal strength can be controlled by adjusting the percentage p, which defines the fraction of quarks participating in the CME-like charge separation. The percentage p is defined as follows:

$$p = \frac{\left(N_{\uparrow}^{+} + N_{\downarrow}^{-}\right) - \left(N_{\downarrow}^{+} + N_{\uparrow}^{-}\right)}{\left(N_{\uparrow}^{+} + N_{\downarrow}^{-}\right) + \left(N_{\downarrow}^{+} + N_{\uparrow}^{-}\right)}, \tag{1}$$

where N is the number of quarks of a given species (u, d, or s). $N_{\uparrow}^{+}$: Number of positively charged quarks moving parallel (↑) to the magnetic field. $N_{\downarrow}^{-}$: Number of negatively charged quarks moving anti-parallel (↓) to the magnetic field. $N_{\downarrow}^{+}$: Number of positively charged quarks moving anti-parallel (↓) to the magnetic field. $N_{\uparrow}^{-}$: Number of negatively charged quarks moving parallel (↑) to the magnetic field.

2.2 Spectator and participant planes

The two-plane method utilizes distinct plane correlations, that is, the elliptical flow-driven background is predominantly correlated with the PP, whereas the CME signal exhibits a stronger correlation with the SP [60, 61]. The SP and PP can be reconstructed using the following equations:

$$\psi_{\mathrm{SP}} = \frac{\mathrm{atan2}\left(\left\langle r_{\mathrm{n}}^{2}\sin\left(2\phi_{\mathrm{n}}\right)\right\rangle, \left\langle r_{\mathrm{n}}^{2}\cos\left(2\phi_{\mathrm{n}}\right)\right\rangle\right)}{2}, \tag{2}$$

$$\psi_{\mathrm{PP}} = \frac{\mathrm{atan2}\left(\left\langle r_{\mathrm{p}}^{2}\sin\left(2\phi_{\mathrm{p}}\right)\right\rangle, \left\langle r_{\mathrm{p}}^{2}\cos\left(2\phi_{\mathrm{p}}\right)\right\rangle\right) + \pi}{2}, \tag{3}$$

where r_{n} and ϕ_{n} represent the displacement and azimuthal angle of the spectator neutrons in the transverse plane, respectively, whereas r_{p} and ϕ_{p} represent the displacement and azimuthal angle of the participating partons in the transverse plane, respectively. All spatial information regarding the displacement and azimuthal angle was obtained from the initial state of the AMPT model. ⟨...⟩ means averaged over all corresponding particles for each event. The PP can be experimentally determined using the event plane reconstructed from final-state hadrons [76]. In this study, the PP was employed to minimize the non-flow effect [37] in the reconstructed ψ_{EP}. However, we systematically verified that all conclusions remained quantitatively consistent when the event plane (EP) method was employed. The corresponding elliptic flow coefficients, $v_2\{\mathrm{SP}\}$ and $v_2\{\mathrm{PP}\}$, using the SP (ψ_{SP}) and PP (ψ_{PP}) methods, respectively, are as follows:

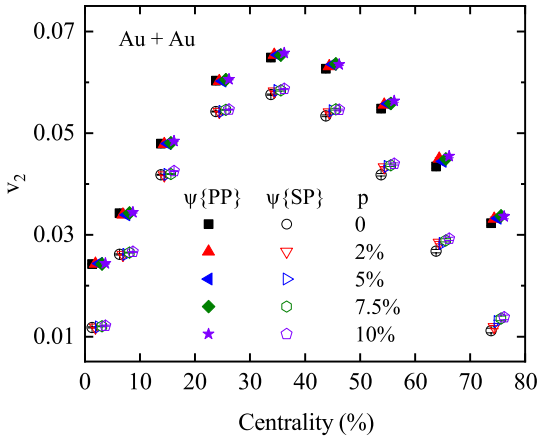

Fig. 1 (Color online) AMPT results on centrality dependence of elliptic flow $v_2\{\mathrm{PP}\}$ (solid symbols) and $v_2\{\mathrm{SP}\}$ (open symbols) in Au+Au collisions at $\sqrt{s_{\mathrm{NN}}} = 200$ GeV from the AMPT model with different strengths of the CME. The data points are shifted along the x axis for clarity

$$v_2\{\mathrm{SP}\} = \left\langle\left\langle\cos 2\left(\phi - \psi_{\mathrm{SP}}\right)\right\rangle\right\rangle, \tag{4}$$

$$v_2\{\mathrm{PP}\} = \left\langle\left\langle\cos 2\left(\phi - \psi_{\mathrm{PP}}\right)\right\rangle\right\rangle. \tag{5}$$

where ϕ represents the azimuthal angle of the final hadrons in the transverse momentum plane, and ⟨⟨...⟩⟩ means averaged over all charged hadrons for all events. Because the PP in experiments is reconstructed using the momenta of final-state particles, it often introduces non-flow contributions to the experimental measurements of $v_2\{\mathrm{PP}\}$ [76]. However, our PP is theoretically reconstructed based on the initial parton positions using Eq. (3), which significantly suppresses the non-flow effect [77, 78]. The self-correlation is also significantly reduced because the dynamic evolution of heavy-ion collisions largely breaks the correlation between the final-state hadrons and our initial-state participant parton plane [77, 78].

Figure 1 presents the centrality dependence of $v_2\{\mathrm{PP}\}$ and $v_2\{\mathrm{SP}\}$ for charged hadrons with $0.2 < p_T < 2.0$ GeV/c and $|\eta| < 1$, obtained from the AMPT model with varying CME strengths in Au+Au collisions at $\sqrt{s_{\mathrm{NN}}} = 200$ GeV. As anticipated, $v_2\{\mathrm{PP}\}$ is consistently larger than $v_2\{\mathrm{SP}\}$ in all cases, because the elliptical flow is more strongly correlated with the PP than with the SP. The values of both $v_2\{\mathrm{PP}\}$ and $v_2\{\mathrm{SP}\}$ increase slightly with p for the peripheral collisions. This is because our CME is introduced by reversing the fraction p of the parton momenta, while preserving their spatial positions. This approach intentionally maintains the initial-state geometry but introduces initial-state residual momentum anisotropy. This initial flow likely couples with the final-state interactions, leading to an increase in the elliptical flow v_2 with p for the peripheral collisions [79].

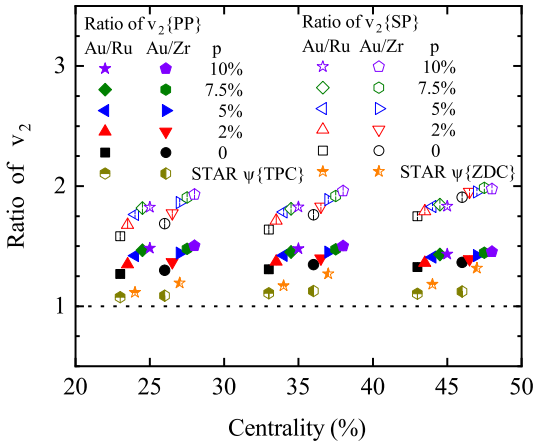

Fig. 2 (Color online) Centrality dependence of elliptic flow $v_2\{\mathrm{PP}\}$ (solid symbols) and $v_2\{\mathrm{SP}\}$ (open symbols) ratios of Au+Au collisions to Ru+Ru and Zr+Zr collisions, respectively, at $\sqrt{s_{\mathrm{NN}}} = 200$ GeV from the AMPT model with different strengths of the CME, in comparison with the STAR data [32, 80]. The data points are shifted along the x axis for clarity

Figure 2 shows the ratios of $v_2\{\mathrm{PP}\}$ and $v_2\{\mathrm{SP}\}$ for Au+Au collisions relative to Ru+Ru and Zr+Zr collisions. Note that all the calculations for the Ru+Ru and Zr+Zr collisions were taken from Ref. [64]. Because the CME is more likely to occur at centrality bins of 20–50%, and to avoid large errors, the comparison is restricted to these centrality bins. The ratio of $v_2\{\mathrm{PP}\}$ is larger than that of $v_2\{\mathrm{SP}\}$, which is consistent with the experimental trends. Compared with the experimental data, a relatively larger ratio in our results arises because the $v_2\{\mathrm{PP}\}$ and $v_2\{\mathrm{SP}\}$ values calculated from our isobar collision simulations are smaller than the experimental results. Similarly, the $v_2\{\mathrm{PP}\}$ and $v_2\{\mathrm{SP}\}$ ratios of Au+Au to Ru+Ru collisions are smaller than those of Au+Au to Zr+Zr collisions, reflecting the influence of the nuclear structure. This indicates that the $v_2\{\mathrm{PP}\}$ and $v_2\{\mathrm{SP}\}$ values for Ru+Ru collisions are larger than those for Zr+Zr collisions owing to the nuclear structure effect [54, 64]. In the 20–50% centrality bin, the changes in $v_2\{\mathrm{PP}\}$ and $v_2\{\mathrm{SP}\}$ values for Au+Au collisions are mere; however, in isobar collisions, the $v_2\{\mathrm{PP}\}$ and $v_2\{\mathrm{SP}\}$ values decrease with increasing p [64], resulting in an increase in the $v_2\{\mathrm{PP}\}$ and $v_2\{\mathrm{SP}\}$ ratios with the strength of the CME.

2.3 Two-plane method to extract f_{CME}

This subsection presents the original two-plane method for detecting and extracting the fraction of the CME signal and its optimization using the AMPT model. The experimentally measurable CME observable, denoted as $\Delta\gamma$, consists of the CME signal and background effect. These background effects are predominantly attributed to the elliptic flow and non-flow effects, which originate from the resonance decays and jet correlations. Consequently, the experimentally measured observable with respect to different planes can be mathematically expressed as the sum of two components:

$$\Delta\gamma\{\psi\} = \Delta\gamma_{\mathrm{Bkg}}\{\psi\} + \Delta\gamma_{\mathrm{CME}}\{\psi\}, \tag{6}$$

where ψ represents either the SP (ψ_{SP}) or PP (ψ_{PP}). The ratios of the elliptical flow and the measured observable with respect to the two different planes are defined as a and A, respectively, as follows:

$$a = v_2\{\mathrm{SP}\}/v_2\{\mathrm{PP}\}, \tag{7}$$

$$A = \Delta\gamma\{\mathrm{SP}\}/\Delta\gamma\{\mathrm{PP}\}. \tag{8}$$

The parameter a is expected to be governed by the two-plane correlation factor, which can be quantitatively expressed by the following relationship: $a = \left\langle \cos 2\left(\psi_{\mathrm{PP}} - \psi_{\mathrm{SP}}\right)\right\rangle$ [60, 81, 82]. Through a straightforward mathematical transformation, the fractional contribution of the CME signal to the total measured observable, denoted by f_{CME}, can be expressed as

$$f_{\mathrm{CME}} = \frac{\Delta\gamma_{\mathrm{CME}}\{\mathrm{PP}\}}{\Delta\gamma\{\mathrm{PP}\}} = \frac{A/a - 1}{1/a^2 - 1}. \tag{9}$$

Equation (9) indicates that the fraction of the CME signal within the measured observable CME can be determined by measuring A and a. However, as noted in Refs. [37, 63], a potential discrepancy may exist between the ratio of the CME signal and inverse ratio of the elliptic flow. This discrepancy was quantitatively verified using our recent AMPT calculations for isobar collisions [64]. Therefore, in a more general case, the following relationship holds:

$$\Delta\gamma_{\mathrm{CME}}\{\mathrm{PP}\} = b\Delta\gamma_{\mathrm{CME}}\{\mathrm{SP}\}. \tag{10}$$

where b represents the ratio of the CME signals with respect to the different planes. Thus, the following equation was derived:

$$\Delta\gamma\{\mathrm{SP}\} = a\Delta\gamma_{\mathrm{Bkg}}\{\mathrm{PP}\} + \frac{\Delta\gamma_{\mathrm{CME}}\{\mathrm{PP}\}}{b}. \tag{11}$$

After accounting for b, a more realistic estimation of the fraction of the CME signal to the total observable signal can be expressed using the following modified relation:

$$f_{\mathrm{CME}}\{b\} = \frac{\Delta\gamma_{\mathrm{CME}}\{\mathrm{PP}\}}{\Delta\gamma\{\mathrm{PP}\}} = \frac{A/a - 1}{1/ab - 1}. \tag{12}$$

The remaining task is to calculate b, which can be theoretically determined. In the AMPT model, the CME signal is simulated by introducing a certain percentage p of partons in the initial state to participate in the charge separation phenomenon. Therefore, the value of b can be determined in the AMPT model using the following relation:

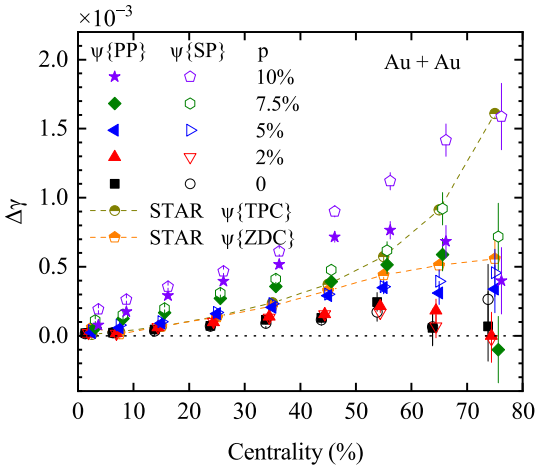

Fig. 3 (Color online) Centrality dependence of $\Delta\gamma\{\mathrm{PP}\}$ (solid symbols) and $\Delta\gamma\{\mathrm{SP}\}$ (open symbols) in Au+Au collisions at $\sqrt{s_{\mathrm{NN}}} = 200$ GeV from the AMPT model with different strengths of the CME, in comparison with the STAR data linked with the dotted line [32]. The data points are shifted along the x axis for clarity

$$b = \frac{\Delta\gamma\{\mathrm{PP}\}(p \neq 0) - \Delta\gamma\{\mathrm{PP}\}(p = 0)}{\Delta\gamma\{\mathrm{SP}\}(p \neq 0) - \Delta\gamma\{\mathrm{SP}\}(p = 0)}, \tag{13}$$

where the numerator and denominator represent the CME signals within the measured CME observable with respect to the PP and SP, respectively.

3 Results and discussion

This section presents the AMPT model results, focusing on the charge-dependent azimuthal correlations for charged particles relative to both the SP and PP. For comparison with the measurements from the STAR experiment, we used kinetic cuts of $0.2 < p_{\mathrm{T}} < 2.0$ GeV/c and $|\eta| < 1$, which are consistent with the STAR experimental setup.

Figure 3 shows the centrality dependence of $\Delta\gamma\{\mathrm{PP}\}$ and $\Delta\gamma\{\mathrm{SP}\}$ from the AMPT model with varying CME strengths in Au+Au collisions at $\sqrt{s_{\mathrm{NN}}} = 200$ GeV. Compared with the STAR data, the CME signal percentage at $p = 5\%$ or 7.5% aligns more closely with the experimental results. Notably, $\Delta\gamma\{\mathrm{SP}\}$ exceeds $\Delta\gamma\{\mathrm{PP}\}$, indicating that the SP serves as a more sensitive probe for the CME because of its stronger correlation with the magnetic field direction compared with the PP.

Figure 4a and b presents the centrality dependence of the $\Delta\gamma\{\mathrm{PP}\}$ and $\Delta\gamma\{\mathrm{SP}\}$ ratios for Au+Au collisions relative to the Ru+Ru and Zr+Zr collisions, respectively. Considering the effect of errors, both the experimental and theoretical results indicate that the $\Delta\gamma$ value for Au+Au collisions is smaller than that for isobar collisions, because most of the ratios are less than one. For the ratio of $\Delta\gamma\{\mathrm{PP}\}$ in Fig. 4a, the AMPT results without the CME signal agree closely with the experimental results, whereas for the ratio $\Delta\gamma\{\mathrm{SP}\}$ in Fig. 4b, the AMPT results with the CME signal show better agreement with the experimental results. As the CME signal correlates more strongly with the SP than with the PP, we observe that the ratio of $\Delta\gamma\{\mathrm{SP}\}$ in Fig. 4b decreases with increasing CME strength. This suggests that $\Delta\gamma\{\mathrm{SP}\}$ in isobar collisions increases more rapidly than that in Au+Au collisions as the CME strength increases.

Figure 5 shows the centrality dependence of $A = \Delta\gamma\{\mathrm{SP}\}/\Delta\gamma\{\mathrm{PP}\}$ and $a = v_2\{\mathrm{SP}\}/v_2\{\mathrm{PP}\}$ from the AMPT model with varying CME strengths, compared with STAR experimental data [32]. As the CME strength in the AMPT model increases, the value of a remains nearly constant and is consistently below unity. It is expected that a follows the expectation $a = \langle\cos 2(\psi_{\mathrm{PP}} - \psi_{\mathrm{SP}})\rangle \approx v_2\{\mathrm{SP}\}/v_2\{\mathrm{PP}\}$ [60, 81, 82]. In Fig. 6, we utilized the AMPT model to directly calculate the values of $\langle\cos 2(\psi_{\mathrm{PP}} - \psi_{\mathrm{SP}})\rangle$ and compared them with the results of $v_2\{\mathrm{SP}\}/v_2\{\mathrm{PP}\}$, denoted as a in Fig. 5. We observe that $v_2\{\mathrm{SP}\}/v_2\{\mathrm{PP}\}$ closely follows $\langle\cos 2(\psi_{\mathrm{PP}} - \psi_{\mathrm{SP}})\rangle$ with

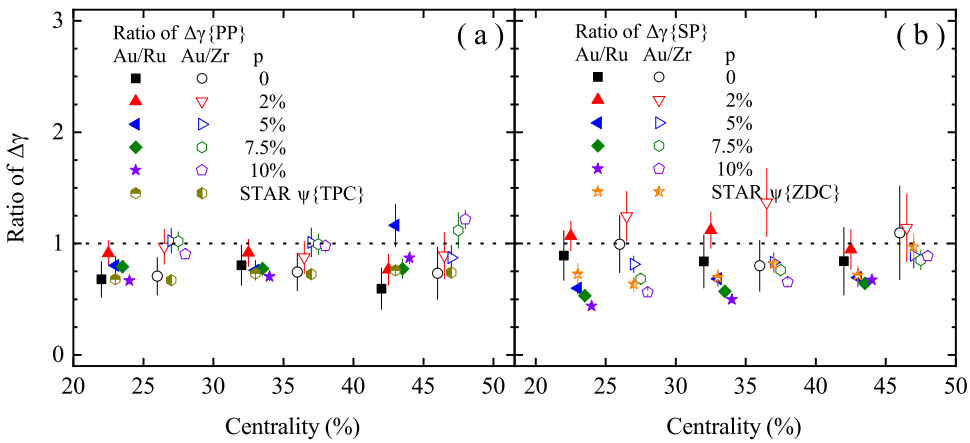

Fig. 4 (Color online) Centrality dependence of $\Delta\gamma\{\mathrm{PP}\}$ **a** and $\Delta\gamma\{\mathrm{SP}\}$ **b** ratios of Au+Au collisions to Ru+Ru collisions (solid symbols) and Zr+Zr collisions (open symbols), respectively, at $\sqrt{s_{\mathrm{NN}}} = 200$ GeV from the AMPT model with different strengths of the CME, in comparison with the STAR data [32, 80]. The data points are shifted along the x axis for clarity

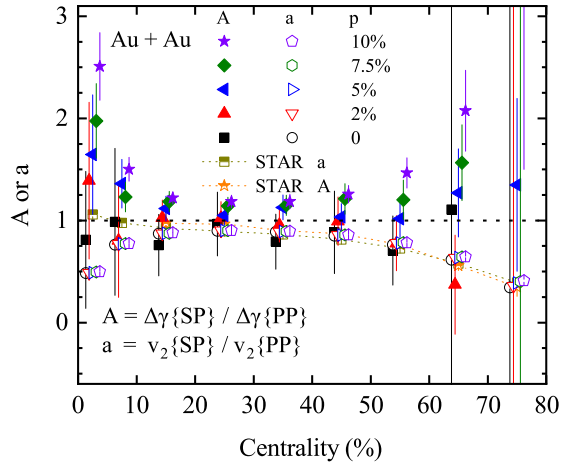

Fig. 5 (Color online) Centrality dependence of A (solid symbols) and a (open symbols) in Au+Au collisions at $\sqrt{s_{\rm NN}} = 200$ GeV from the AMPT model with different strengths of the CME, in comparison with the STAR data linked with the dotted line [32]. The data points are shifted along the x axis for clarity

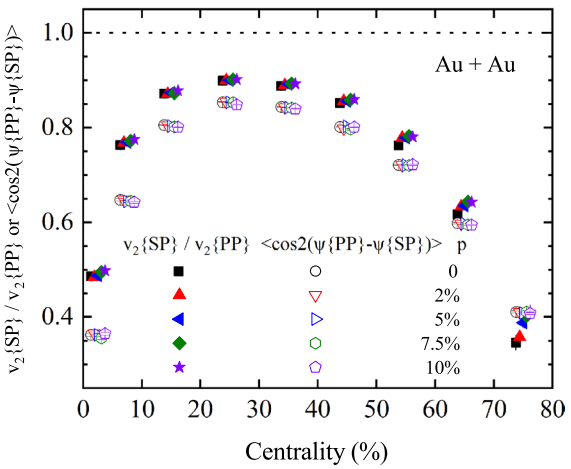

Fig. 6 (Color online) Centrality dependence of $v_2\{\mathrm{SP}\}/v_2\{\mathrm{PP}\}$ (solid symbols) and $\langle\cos 2(\psi_{\rm PP} - \psi_{\rm SP})\rangle$ (open symbols) in Au+Au collisions at $\sqrt{s_{\rm NN}} = 200$ GeV from the AMPT model with different strengths of the CME. The data points are shifted along the x axis for clarity

small differences that can be attributed to non-flow effects. In contrast, the values of A increase with p, suggesting that the CME affects $\Delta\gamma$ differently for the two planes. For small values of p, the model results align more closely with the experimental data.

Figure 7 shows the centrality dependence of the A and a ratios for Au+Au collisions relative to Ru+Ru and Zr+Zr collisions, respectively. The ratio of a remains nearly unchanged, which is consistent with the experimental data within error. An a ratio greater than one indicates that the

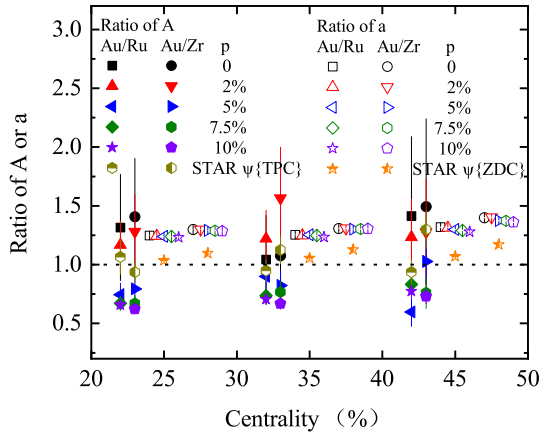

Fig. 7 (Color online) Centrality dependence of A (solid symbols) and a (open symbols) ratios of Au+Au collisions to Ru+Ru and Zr+Zr collisions, respectively, at $\sqrt{s_{\rm NN}} = 200$ GeV from the AMPT model with different strengths of the CME, in comparison with the STAR data [32, 80]. The data points are shifted along the x axis for clarity

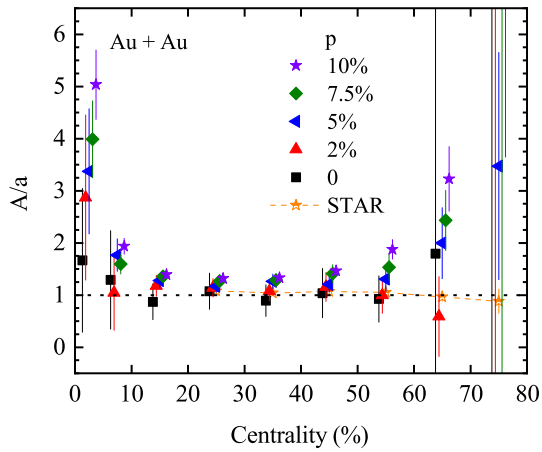

Fig. 8 (Color online) Centrality dependence of A/a in Au+Au collisions at $\sqrt{s_{\rm NN}} = 200$ GeV from the AMPT model with different strengths of the CME, in comparison with the STAR data linked with the dotted line [32]. The data points are shifted along the x axis for clarity

$\langle\cos 2(\psi_{\rm PP} - \psi_{\rm SP})\rangle$ value is larger, implying a smaller difference angle between $\psi_{\rm PP}$ and $\psi_{\rm SP}$ for Au+Au collisions than that for isobar collisions. For larger CME strengths, the ratio of A is less than one, indicating that the ratios of $\Delta\gamma\{\mathrm{SP}\}$ and $\Delta\gamma\{\mathrm{PP}\}$ are smaller in Au+Au collisions than in isobar collisions, that is, $\Delta\gamma\{\mathrm{SP}\}$ and $\Delta\gamma\{\mathrm{PP}\}$ are closer in Au+Au collisions than those in isobar collisions.

Figure 8 shows A/a as a function of the centrality predicted by the AMPT model with varying CME strengths. According to Eqs. (9) and (12), A/a values greater than unity indicate the presence of a CME signal within the $\Delta\gamma$ observable. Focusing on mid-central collisions (20–50%

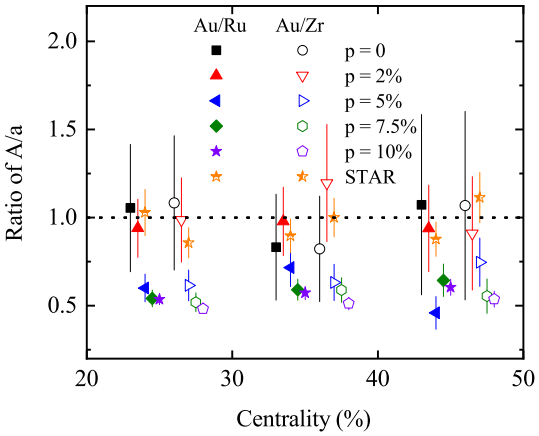

Fig. 9 (Color online) Centrality dependence of A/a ratios of Au+Au collisions to Ru+Ru and Zr+Zr collisions, respectively, at $\sqrt{s_{\rm NN}} = 200$ GeV from the AMPT model with different strengths of the CME, in comparison with the STAR data [32, 80]. The data points are shifted along the x axis for clarity

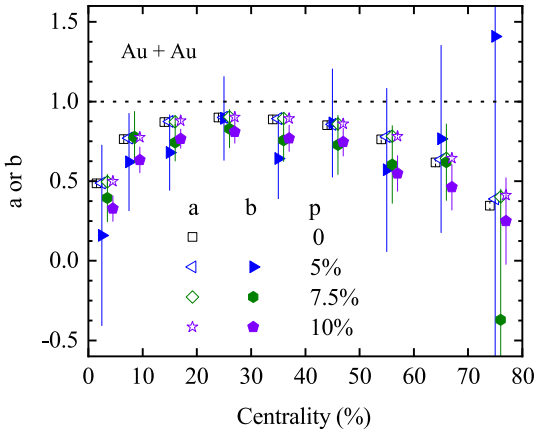

Fig. 10 (Color online) AMPT results on centrality dependence of a (solid symbols) and b (open symbols) in Au+Au collisions at $\sqrt{s_{\rm NN}} = 200$ GeV from the AMPT model with different strengths of the CME. The data points are shifted along the x axis for clarity

centrality), where the CME effect is more measurable, $A/a > 1$ is observed for all cases except when $p = 0$ and $p = 2\%$. Notably, A/a increases with CME strength, suggesting that this ratio reflects the strength of the CME signal. The experimental data are closer to the cases with lower strengths of the CME signal.

Figure 9 shows the centrality dependence of the A/a ratios for Au+Au collisions relative to Ru+Ru and Zr+Zr collisions. Focusing on mid-central collisions (20–50% centrality), the A/a ratios for the Au+Au and isobar collisions exhibit a trend similar to that of the A ratio shown in Fig. 7, driven by a smaller variation in a and larger variation in A. The experimental data are also closer to the cases with lower strengths of the CME signal.

Figure 10 shows the centrality dependence of a and b calculated using Eq. (13), based on the AMPT model with varying CME strengths. Notably, a and b exhibit significant differences. In the 20–50% centrality bins, b remains consistently smaller than a. Moreover, a shows minimal dependence on CME strength, as presented in Fig. 5. By contrast, b reflects the capability of the PP method to capture the CME signal observed in the SP method. Although the statistical errors are substantial, b shows no significant variation with CME strengths, except for the 2% CME strength case, which is excluded because of its large statistical uncertainties.

Figure 11 shows the centrality dependence of the a and b ratios for Au+Au collisions relative to Ru+Ru and Zr+Zr collisions, respectively, based on the AMPT model with various CME strengths. Focusing on the 20–50% centrality bins, the a ratio remains nearly unchanged and is smaller than the b ratio. The uncertainties of b ratios are large. According to Eq. (13), a larger b value indicates a smaller difference in the net CME strength between the two planes. Therefore, our results indicate that the difference is smaller in Au+Au collisions than in isobar collisions.

Figure 12 shows the centrality dependence of the b/a ratio as predicted by the AMPT model with varying CME strengths. Focusing on the 20–50% centrality bins in Au+Au collisions at $\sqrt{s_{\rm NN}} = 200$ GeV, the b/a ratio can be approximated by using a constant function, yielding $b/a = 0.88(\pm 0.08)$. Our previous study shows that isobar collisions yield $b/a = 0.65(\pm 0.18)$ [64]. This result implies that the relative ratio of CME signals across different planes does not simply invert the elliptical flow ratio among these planes. This finding has significant implications for extracting the fraction of the CME signal

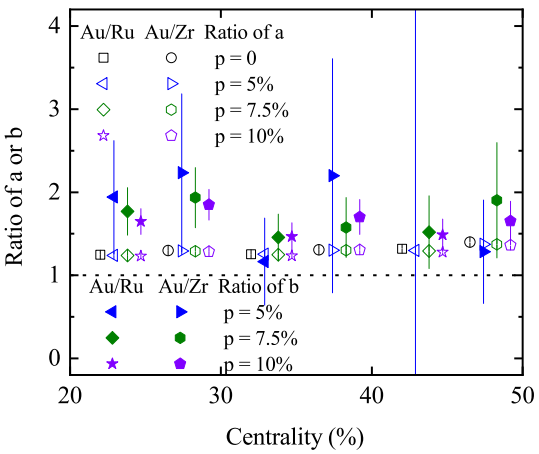

Fig. 11 (Color online) AMPT results on centrality dependence of the a (open symbols) and b (solid symbols) ratios of Au+Au collisions to Ru+Ru and Zr+Zr collisions, respectively, at $\sqrt{s_{\rm NN}} = 200$ GeV from the AMPT model with different strengths of the CME. The data points are shifted along the x axis for clarity

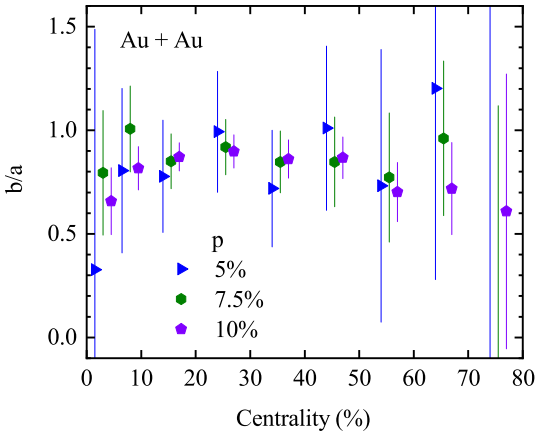

Fig. 12 (Color online) Centrality dependence of b/a in Au+Au collisions at $\sqrt{s_{\rm NN}} = 200$ GeV from the AMPT model with different strengths of the CME. The data points are shifted along the x axis for clarity

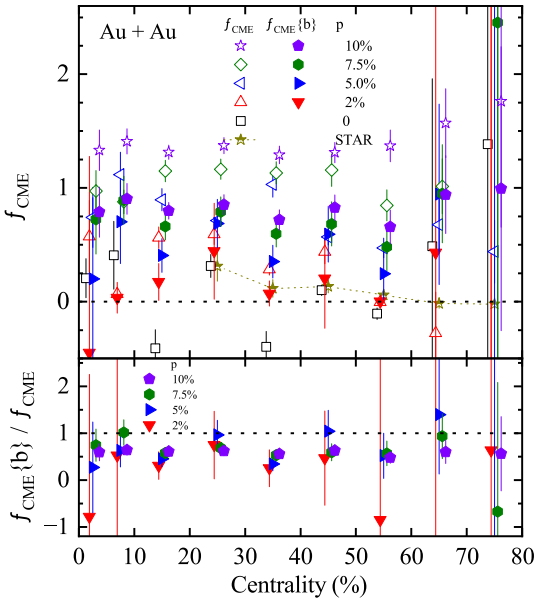

Fig. 14 (Color online) Upper panel: Centrality dependence of $f_{\rm CME}\{b\}$ and $f_{\rm CME}$ in Au+Au collisions at $\sqrt{s_{\rm NN}} = 200$ GeV from the AMPT model with different strengths of the CME, in comparison with the STAR data [32]. The solid and open symbols represent the results for $f_{\rm CME}\{b\}$ and $f_{\rm CME}$, respectively. Lower panel: Centrality dependence of the ratio of $f_{\rm CME}\{b\}$ to $f_{\rm CME}$. The data points are shifted along the x axis for clarity

within the $\Delta\gamma$ observable, which will be discussed further.

Figure 13 shows the centrality dependence of b/a for Au+Au collisions relative to Ru+Ru and Zr+Zr collisions, respectively, based on the AMPT model with varying CME strengths. Because the value of a remains nearly constant, the ratio b/a follows the trend of the ratio b shown in Fig. 11. The same p input is employed for each centrality in Figs. 11 and 13. However, it should be pointed out that as the magnetic field is expected to be stronger for Au+Au collisions than for isobaric collisions at the same centrality, the p values should differ for these systems.

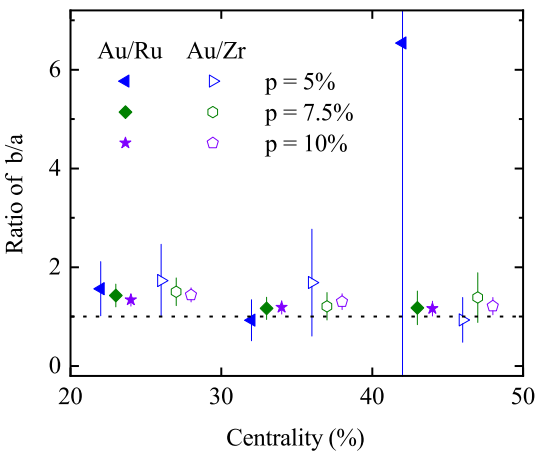

Fig. 13 (Color online) Centrality dependence of the b/a ratios of Au+Au collisions to Ru+Ru and Zr+Zr collisions, respectively, at $\sqrt{s_{\rm NN}} = 200$ GeV from the AMPT model with different strengths of the CME. The data points are shifted along the x axis for clarity

The upper panel of Fig. 14 shows the centrality dependence of the two types of $f_{\rm CME}$ based on the AMPT model with varying CME strengths. The open and solid symbols represent $f_{\rm CME}$ and $f_{\rm CME}\{b\}$ calculated using Eqs. (9) and (12), respectively. Our results are consistent with the STAR experimental data [32], favoring the cases of $p = 0\%$ and $p = 2\%$. Notably, for the 20–50% centrality bins, when $p \neq 0$, $f_{\rm CME}\{b\}$ is smaller than $f_{\rm CME}$. The negative $f_{\rm CME}$ values at $p = 0\%$ arise from statistical fluctuations in the baseline measurement. The lower panel of Fig. 14 shows the centrality dependence of the ratio $f_{\rm CME}\{b\}$ to $f_{\rm CME}$, which is less than unity for–20–50% centrality bins. This implies that assuming $b = a$ leads to an overestimation of the CME signal fraction within the $\Delta\gamma$ observable.

Figure 15 shows the $f_{\rm CME}$, $f_{\rm CME}\{b\}$, and $f_{\rm CME}\{p\}$ ratios for Au+Au collisions relative to Ru+Ru and Zr+Zr collisions, respectively, in the 20–50% centrality bins at $\sqrt{s_{\rm NN}} = 200$ GeV. Note that the STAR data for the Ru+Ru and Zr+Zr collisions were obtained by averaging the data reported in Ref [80], which indicates that without accounting for the effect of b, the fraction of CME signals in $\Delta\gamma$ is slightly larger in isobar collisions than in Au+Au collisions. The $f_{\rm CME}\{p\}$ ratio was calculated using the method described in Ref. [64]. $f_{\rm CME}\{p\}$ is defined as follows:

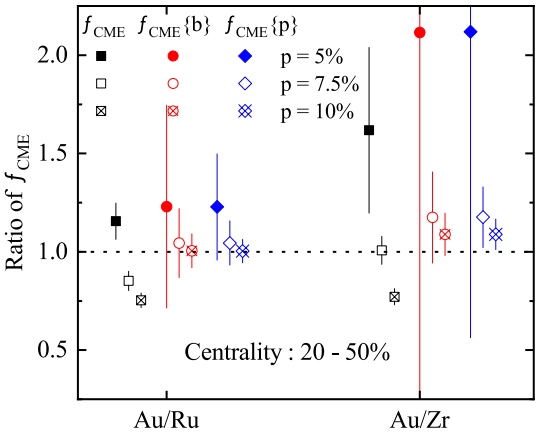

Fig. 15 (Color online) f_{CME}, $f_{CME}\{b\}$, and $f_{CME}\{p\}$ ratios of Au+Au collisions to Ru+Ru and Zr+Zr collisions, respectively, in 20–50% centrality bins at $\sqrt{s_{NN}} = 200$ GeV from the AMPT model with different strengths of the CME. The solid, open symbols, and open symbols with X represent the results for the AMPT model with different strengths of the CME in comparison with the STAR data [32, 80]. The data points are shifted along the x axis for clarity

$$f_{CME}\{p\} = \frac{\Delta\gamma_{CME}\{PP\}(p \neq 0)}{\Delta\gamma\{PP\}(p \neq 0)}, \tag{14}$$

where

$$\Delta\gamma_{CME}\{PP\}(p \neq 0) = \Delta\gamma\{PP\}(p \neq 0) - \Delta\gamma\{PP\}(p = 0). \tag{15}$$

The observables $\Delta\gamma\{PP\}(p = 0)$ and $\Delta\gamma\{PP\}(p \neq 0)$ can be obtained from the AMPT model without the CME and with different strengths of the CME, respectively. However, the ratio of Au+Au collisions relative to isobar collisions increases after applying the correction for b, which indicates that, after accounting for b, the fraction of CME signals in $\Delta\gamma$ is greater for Au+Au collisions than for isobar collisions. Therefore, it is important to consider the effect of b to achieve real facts about the CME.

As the introduced CME signal strength increases, the ratios calculated using all the three methods decrease. This is because the A/a value increases more significantly in isobar collisions than in Au+Au collisions, leading to a reduction in the calculated ratios. It is also observed that the Au/Ru ratio is smaller than the Au/Zr ratio in the presence of CME signals, indicating that the fraction of CME signal is higher in Ru+Ru than in Zr+Zr.

The preceding results demonstrate that the ratio $b/a = 0.88(\pm 0.08)$ significantly influences the final result of f_{CME} in the 20–50% centrality bins for Au+Au collisions. To elucidate the origin of this relationship, we investigated the evolution of a and b at different stages of the Au+Au collisions at $\sqrt{s_{NN}} = 200$ GeV in the AMPT model, assuming a CME strength of $p = 10\%$. We focused on four distinct stages: the initial stage, after parton cascade, after coalescence, and after hadron rescatterings. As shown in the upper panel of Fig. 16, the value of a remained constant during the last three stages. The initial stage is excluded from the a calculation because the elliptical flow is initially zero. In contrast, the value of b is consistently smaller than a and decreases with each stage in the 20–50% centrality bins. The lower panel of Fig. 16 illustrates the decreasing trend of the b/a ratio during the evolution stage, which is primarily driven by a decrease in b. This decrease in b suggests weaker correlation between CME signals across different planes, which can be attributed to the effects of final-state interactions during the evolution of heavy-ion collisions [54, 75, 83, 84].

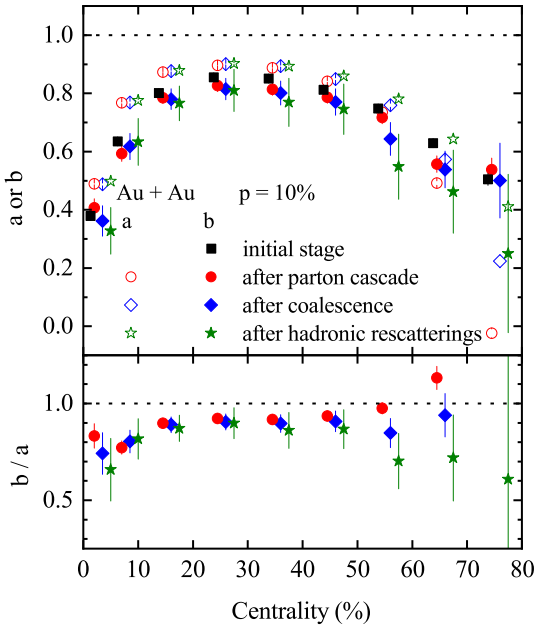

Fig. 16 (Color online) Upper panel: Centrality dependence of a and b in Au+Au collisions at $\sqrt{s_{NN}} = 200$ GeV for four different stages of the AMPT model with a CME strength of $p = 10\%$. The open and solid symbols represent the results for a and b, respectively. Lower panel: centrality dependence of the ratio b/a for the different stages in Au+Au collisions. The same symbols as b in the upper panel are used to indicate different stages. The data points are shifted along the x axis for clarity

In Ref. [75], the authors demonstrated that the final-state interactions in relativistic heavy-ion collisions significantly suppress the initial charge separation, with a reduction factor reaching up to an order of magnitude. In our previous work [64], we found that, because of the anisotropic overlap zone, these interactions not only reduce the magnitude of the CME current but also alter its direction, resulting in a modified maximum current orientation. Figure 17 shows the centrality dependence of the b/a ratio in the Ru+Ru [64] and Au+Au collisions at $\sqrt{s_{NN}} = 200$ GeV for different stages in the AMPT model with a CME

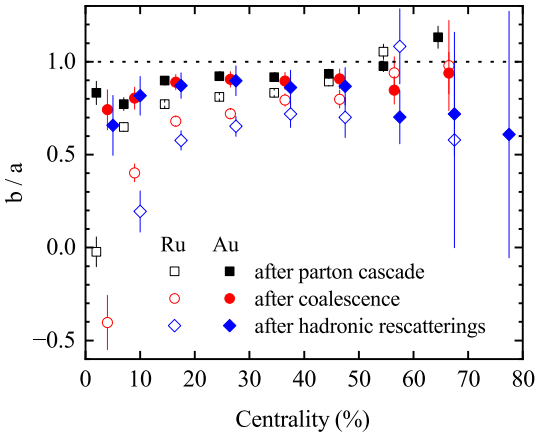

Fig. 17 (Color online) Centrality dependence of the ratio of b/a in Ru+Ru [64] and Au+Au collisions at $\sqrt{s_{\rm NN}} = 200$ GeV for different stages from the AMPT model with the CME strength of $p = 10\%$. The open and solid symbols represent the results for Ru+Ru and Au+Au, respectively. The data points are shifted along the x axis for clarity

strength of $p = 10\%$. For the 20–50% centrality bins, the b/a ratios show a decreasing trend with the stage evolution for both Ru+Ru and Au+Au collisions. Furthermore, the b/a values for Ru+Ru collisions are consistently smaller than those for Au+Au collisions across different stages and decrease more rapidly. This observation implies that the effect of the final-state interactions on the decorrelation of CME signals relative to the SP and PP is less pronounced in Au+Au collisions, making it more favorable to detect CME signals using the two-plane method. In our previous AMPT study [64, 75], we showed that assuming $b = a$ in isobar collisions overestimates the final-state CME fraction in the measured $\Delta\gamma$ observable because the signal is subsequently damped and washed out during the final-state evolution of relativistic heavy-ion collisions. We found that $b/a = 0.88 \pm 0.08$ was larger in Au+Au collisions than in isobar collisions at the same centrality ($b/a = 0.65 \pm 0.18$), indicating that the signal was damped and washed out to a lesser extent in Au+Au collisions than in isobar collisions.

To constrain the CME strengths across Au+Au and isobar collisions simultaneously, we performed a chi-square analysis using the following method. We aimed to compare the CME observable between our results with different CME strengths and the experimental data for those three collision systems simultaneously. The chi-square for a CME observable O in centrality bin i is defined as follows:

$$\chi^2 = \sum_{k=0}^{n} \frac{\left(O_i - E_i\right)^2}{w_o^2}, \tag{16}$$

where we select the CME observable of O_i as the double ratio between Au+Au and isobar collisions to reduce the effect of the background.

$$O_i = \frac{\frac{\{\Delta\gamma(\psi)\}_{\rm Au}}{\{v_2(\psi)\}_{\rm Au}} \times \{{\rm d}N_{\rm ch}/{\rm d}\eta\}_{\rm Au}}{\frac{\{\Delta\gamma(\psi)\}_{\rm Isobar}}{\{v_2(\psi)\}_{\rm Isobar}} \times \{{\rm d}N_{\rm ch}/{\rm d}\eta\}_{\rm Isobar}}, \tag{17}$$

where ψ is $\psi_{\rm PP}$ or $\psi_{\rm SP}$, and ${\rm d}N_{\rm ch}/{\rm d}\eta$ denotes the number of charged particles. E_i represents experimental results. w_o^2 represents the error in the calculation results of O_i, and i denotes in the 20–50% centrality bin. Figure 18 shows the results of the two-dimensional normalized chi-square distribution with respect to the different CME signal strengths in Au+Au collisions and the different CME signal strengths in isobar collisions. For the PP plane cases shown in panels (a) and (c), the AMPT simulation results align most closely with the experimental data when the CME strengths for Au+Au, Ru+Ru, and Zr+Zr collisions are all close to 2%. This indicates that, for the PP plane, the experimental results tend to exhibit small CME signals for all three collision systems because the CME signal in the PP plane is relatively insensitive to the SP plane. However, for the SP plane cases shown in panels (b) and (d), the AMPT simulation results align most closely with the experimental data when the CME strength in Au+Au collisions is 7.5% and that in Ru+Ru collisions is 5%, or when the CME strength in Au+Au collisions is 10% and that in Zr+Zr collisions is 7.5%. This indicates that the experimental results for the SP plane tend to exhibit larger CME signals than those for the PP plane for all three collision systems, with stronger signals observed in Au+Au collisions than in isobar collisions because the CME signal exhibits greater sensitivity to the SP plane than to the PP plane.

4 Summary

Using a multiphase transport model with varying CME strengths, we extended our two-plane method analysis from isobar to Au+Au collisions, both at $\sqrt{s_{\rm NN}} = 200$ GeV. Our previous isobar collision studies revealed a significant difference ($b/a = 0.65 \pm 0.18$) in the CME signal-to-background ratio between the two planes, complicating CME signal extraction in isobar collisions [64]. However, the current Au+Au analysis demonstrated a reduced difference ($b/a = 0.88 \pm 0.08$) in the CME signal-to-background ratio between the two planes, which enhanced the experimental reliability of the two-plane method for the measurement of Au+Au collisions. Through comprehensive chi-square analysis across the three collision systems, we established that Au+Au collisions exhibit stronger CME signatures compared with isobar

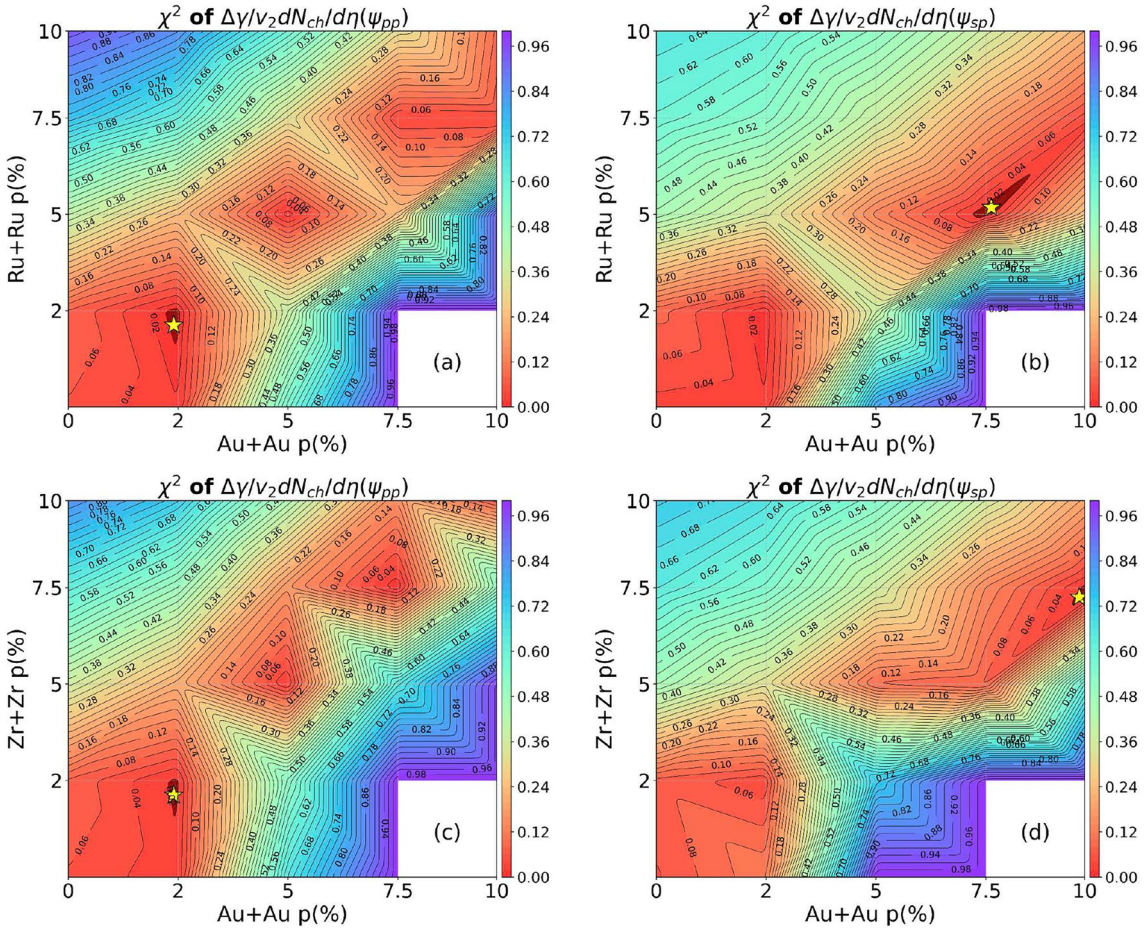

Fig. 18 (Color online) Two-dimensional normalized chi-square distribution with respect to the different CME signal strengths in Au+Au collisions and the different CME signal strengths in isobar collisions. The chi-square (χ^2) value represents the goodness of how well our model describes the experimental data for the CME observable of $\Delta\gamma/v_2 dN_{ch}/d\eta$. The panels **a** and **b** show the results between Au+Au collisions and Ru+Ru collisions with respect to ψ_{PP} and ψ_{SP}, respectively. The panels **c** and **d** show the results between Au+Au collisions and Zr+Zr collisions with respect to ψ_{PP} and ψ_{SP}, respectively. Note that the magnitudes of the normalized chi-square value vary with color, where the dark red region, highlighted as a pentagram, indicates the smallest χ^2 value, which corresponds to the best description

systems, which is consistent with a simple picture: Au+Au collisions should have a larger magnetic field because there are more protons [11, 43, 62], particularly when analyzed with respect to the SP. These findings not only validate the improved applicability of the two-plane method in Au+Au collisions but also provide critical insights into the system size dependence of the CME observable, advancing our future experimental measurements of the CME.

Acknowledgements We thank Prof. Fuqiang Wang and Jie Zhao for their helpful discussions.

Declarations

Conflict of interest The authors declare that they have no Conflict of interest.

References

1. P.F. Kolb, J. Sollfrank, U.W. Heinz, Anisotropic transverse flow and the quark hadron phase transition. Phys. Rev. C **62**, 054909 (2000). arXiv:hep-ph/0006129, https://doi.org/10.1103/PhysRevC.62.054909
2. D. Teaney, J. Lauret, E.V. Shuryak, Flow at the SPS and RHIC as a quark gluon plasma signature. Phys. Rev. Lett. **86**, 4783–4786 (2001). https://doi.org/10.1103/PhysRevLett.86.4783
3. L. Yan, A flow paradigm in heavy-ion collisions. Chin. Phys. C **42**, 042001 (2018). https://doi.org/10.1088/1674-1137/42/4/042001
4. C. Shen, L. Yan, Recent development of hydrodynamic modeling in heavy-ion collisions. Nucl. Sci. Tech. **31**, 122 (2020). https://doi.org/10.1007/s41365-020-00829-z
5. H. Song, Y. Zhou, K. Gajdosova, Collective flow and hydrodynamics in large and small systems at the LHC. Nucl. Sci. Tech. **28**, 99 (2017). https://doi.org/10.1007/s41365-017-0245-4

6. S.W. Lan, S.S. Shi, Anisotropic flow in high baryon density region. Nucl. Sci. Tech. **33**, 21 (2022). https://doi.org/10.1007/s41365-022-01006-0
7. S. Wu, C. Shen, H. Song, Dynamically exploring the QCD matter at finite temperatures and densities: a short review. Chin. Phys. Lett. **38**, 081201 (2021). https://doi.org/10.1088/0256-307X/38/8/081201
8. Q.Y. Shou et al., Properties of QCD matter: a review of selected results from ALICE experiment. Nucl. Sci. Tech. **35**, 219 (2024). https://doi.org/10.1007/s41365-024-01583-2
9. V. Skokov, A.Y. Illarionov, V. Toneev, Estimate of the magnetic field strength in heavy-ion collisions. Int. J. Mod. Phys. A **24**, 5925–5932 (2009). https://doi.org/10.1142/S0217751X09047570
10. A. Bzdak, V. Skokov, Event-by-event fluctuations of magnetic and electric fields in heavy ion collisions. Phys. Lett. B **710**, 171–174 (2012). https://doi.org/10.1016/j.physletb.2012.02.065
11. W.T. Deng, X.G. Huang, Event-by-event generation of electromagnetic fields in heavy-ion collisions. Phys. Rev. C **85**, 044907 (2012). https://doi.org/10.1103/PhysRevC.85.044907
12. X.L. Zhao, Y.G. Ma, G.L. Ma, Electromagnetic fields in small systems from a multiphase transport model. Phys. Rev. C **97**, 024910 (2018). https://doi.org/10.1103/PhysRevC.97.024910
13. X.L. Zhao, G.L. Ma, Y.G. Ma, Novel mechanism for electric quadrupole moment generation in relativistic heavy-ion collisions. Phys. Lett. B **792**, 413–418 (2019). https://doi.org/10.1016/j.physletb.2019.04.002
14. Y. Chen, X.L. Sheng, G.L. Ma, Electromagnetic fields from the extended Kharzeev–McLerran-Warringa model in relativistic heavy-ion collisions. Nucl. Phys. A **1011**, 122199 (2021). https://doi.org/10.1016/j.nuclphysa.2021.122199
15. B.X. Chen, S.Q. Feng, A systematical study of the chiral magnetic effects at the RHIC and LHC energies. Chin. Phys. C **44**, 024104 (2020). https://doi.org/10.1088/1674-1137/44/2/024104
16. J. Zhao, J.H. Chen, X.G. Huang et al., Electromagnetic fields in ultra-peripheral relativistic heavy-ion collisions. Nucl. Sci. Tech. **35**, 20 (2024). https://doi.org/10.1007/s41365-024-01374-9
17. D. Kharzeev, Parity violation in hot QCD: Why it can happen, and how to look for it. Phys. Lett. B **633**, 260–264 (2006). https://doi.org/10.1016/j.physletb.2005.11.075
18. D.E. Kharzeev, L.D. McLerran, H.J. Warringa, The Effects of topological charge change in heavy ion collisions: 'event by event P and CP violation'. Nucl. Phys. A **803**, 227–253 (2008). https://doi.org/10.1016/j.nuclphysa.2008.02.298
19. K. Fukushima, D.E. Kharzeev, H.J. Warringa, The chiral magnetic effect. Phys. Rev. D **78**, 074033 (2008). https://doi.org/10.1103/PhysRevD.78.074033
20. S.A. Voloshin, Parity violation in hot QCD: How to detect it. Phys. Rev. C **70**, 057901 (2004). https://doi.org/10.1103/PhysRevC.70.057901
21. B.I. Abelev et al., Azimuthal charged-particle correlations and possible local strong parity violation. Phys. Rev. Lett. **103**, 251601 (2009). https://doi.org/10.1103/PhysRevLett.103.251601
22. B.I. Abelev et al., Observation of charge-dependent azimuthal correlations and possible local strong parity violation in heavy ion collisions. Phys. Rev. C **81**, 054908 (2010). https://doi.org/10.1103/PhysRevC.81.054908
23. L. Adamczyk et al., Fluctuations of charge separation perpendicular to the event plane and local parity violation in $\sqrt{s_{NN}} = 200$ GeV Au+Au collisions at the BNL Relativistic Heavy Ion Collider. Phys. Rev. C **88**, 064911 (2013). https://doi.org/10.1103/PhysRevC.88.064911
24. L. Adamczyk et al., Beam-energy dependence of charge separation along the magnetic field in Au+Au collisions at RHIC. Phys. Rev. Lett. **113**, 052302 (2014). https://doi.org/10.1103/PhysRevLett.113.052302
25. B. Abelev, et al., Charge separation relative to the reaction plane in Pb-Pb collisions at $\sqrt{s_{NN}} = 2.76$ TeV. Phys. Rev. Lett. **110**, 012301 (2013). https://doi.org/10.1103/PhysRevLett.110.012301
26. A. Bzdak, V. Koch, J. Liao, Azimuthal correlations from transverse momentum conservation and possible local parity violation. Phys. Rev. C **83**, 014905 (2011). https://doi.org/10.1103/PhysRevC.83.014905
27. J. Liao, V. Koch, A. Bzdak, On the charge separation effect in relativistic heavy ion collisions. Phys. Rev. C **82**, 054902 (2010). https://doi.org/10.1103/PhysRevC.82.054902
28. S. Schlichting, S. Pratt, Charge conservation at energies available at the BNL relativistic heavy ion collider and contributions to local parity violation observables. Phys. Rev. C **83**, 014913 (2011). https://doi.org/10.1103/PhysRevC.83.014913
29. F. Wang, Effects of cluster particle correlations on local parity violation observables. Phys. Rev. C **81**, 064902 (2010). https://doi.org/10.1103/PhysRevC.81.064902
30. W.Y. Wu et al., Global constraint on the magnitude of anomalous chiral effects in heavy-ion collisions. Phys. Rev. C **107**, L031902 (2023). https://doi.org/10.1103/PhysRevC.107.L031902
31. L. Adamczyk et al., Measurement of charge multiplicity asymmetry correlations in high-energy nucleus-nucleus collisions at $\sqrt{s_{NN}} = 200$ GeV. Phys. Rev. C **89**, 044908 (2014). https://doi.org/10.1103/PhysRevC.89.044908
32. M.S. Abdallah et al., Search for the chiral magnetic effect via charge-dependent azimuthal correlations relative to spectator and participant planes in Au+Au collisions at $\sqrt{s_{NN}} = 200$ GeV. Phys. Rev. Lett. **128**, 092301 (2022). https://doi.org/10.1103/PhysRevLett.128.092301
33. F.Q. Wang, J. Zhao, Search for the chiral magnetic effect in heavy ion collisions. Nucl. Sci. Tech. **29**, 179 (2018). https://doi.org/10.1007/s41365-018-0520-z
34. J. Zhao, F. Wang, Experimental searches for the chiral magnetic effect in heavy-ion collisions. Prog. Part. Nucl. Phys. **107**, 200–236 (2019). https://doi.org/10.1016/j.ppnp.2019.05.001
35. J. Zhao, Search for CME in U+U and Au+Au collisions in STAR with different approaches of handling backgrounds. Nucl. Phys. A **1005**, 121766 (2021). https://doi.org/10.1016/j.nuclphysa.2020.121766
36. F. Wang, CME—experimental results and interpretation. Acta Phys. Polon. Supp. **16**, 1-A15 (2023). https://doi.org/10.5506/APhysPolBSupp.16.1-A15
37. Y. Feng, J. Zhao, H. Li et al., Two- and three-particle nonflow contributions to the chiral magnetic effect measurement by spectator and participant planes in relativistic heavy ion collisions. Phys. Rev. C **105**, 024913 (2022). https://doi.org/10.1103/PhysRevC.105.024913
38. W. Li, G. Wang, Chiral magnetic effects in nuclear collisions. Ann. Rev. Nucl. Part. Sci. **70**, 293–321 (2020). https://doi.org/10.1146/annurev-nucl-030220-065203
39. S. Qi-Ye et al., Progress on the experimental search for the chiral magnetic effect, the chiral vortical effect, and the chiral magnetic wave. Acta Phys. Sin. **72**, 112504 (2023). https://doi.org/10.7498/aps.72.20230109
40. Z. Xu, B. Chan, G. Wang et al., Event shape selection method in search of the chiral magnetic effect in heavy-ion collisions. Phys. Lett. B **848**, 138367 (2024). https://doi.org/10.1016/j.physletb.2023.138367
41. Y.S. Zhao, L. Wang, K. Zhou et al., Detecting the chiral magnetic effect via deep learning. Phys. Rev. C **106**, L051901 (2022). https://doi.org/10.1103/PhysRevC.106.L051901
42. S.A. Voloshin, Testing the chiral magnetic effect with central U+U collisions. Phys. Rev. Lett. **105**, 172301 (2010). https://doi.org/10.1103/PhysRevLett.105.172301

43. W.T. Deng, X.G. Huang, G.L. Ma et al., Test the chiral magnetic effect with isobaric collisions. Phys. Rev. C **94**, 041901 (2016). https://doi.org/10.1103/PhysRevC.94.041901
44. M.I. Abdulhamid et al., Upper limit on the chiral magnetic effect in isobar collisions at the Relativistic Heavy-Ion Collider. Phys. Rev. Res. **6**, L032005 (2024). https://doi.org/10.1103/PhysRevResearch.6.L032005
45. M.I. Abdulhamid et al., Estimate of background baseline and upper limit on the chiral magnetic effect in isobar collisions at sNN=200 GeV at the BNL Relativistic Heavy Ion Collider. Phys. Rev. C **110**, 014905 (2024). https://doi.org/10.1103/PhysRevC.110.014905
46. J. Chen et al., Properties of the QCD matter: review of selected results from the relativistic heavy ion collider beam energy scan (RHIC BES) program. Nucl. Sci. Tech. **35**, 214 (2024). https://doi.org/10.1007/s41365-024-01591-2
47. H.j. Xu, H. Li, X. Wang, et al., Determine the neutron skin type by relativistic isobaric collisions. Phys. Lett. B **819**, 136453 (2021). https://doi.org/10.1016/j.physletb.2021.136453
48. H.j. Xu, W. Zhao, H. Li, et al., Probing nuclear structure with mean transverse momentum in relativistic isobar collisions. Phys. Rev. C **108**, L011902 (2023). https://doi.org/10.1103/PhysRevC.108.L011902
49. C. Zhang, J. Jia, Evidence of quadrupole and octupole deformations in Zr96+Zr96 and Ru96+Ru96 collisions at ultrarelativistic energies. Phys. Rev. Lett. **128**, 022301 (2022). https://doi.org/10.1103/PhysRevLett.128.022301
50. J. Jia, C. Zhang, Scaling approach to nuclear structure in high-energy heavy-ion collisions. Phys. Rev. C **107**, L021901 (2023). https://doi.org/10.1103/PhysRevC.107.L021901
51. G. Giacalone, J. Jia, C. Zhang, Impact of nuclear deformation on relativistic heavy-ion collisions: assessing consistency in nuclear physics across energy scales. Phys. Rev. Lett. **127**, 242301 (2021). https://doi.org/10.1103/PhysRevLett.127.242301
52. J. Jia, Shape of atomic nuclei in heavy ion collisions. Phys. Rev. C **105**, 014905 (2022). https://doi.org/10.1103/PhysRevC.105.014905
53. J. Jia, Probing triaxial deformation of atomic nuclei in high-energy heavy ion collisions. Phys. Rev. C **105**, 044905 (2022). https://doi.org/10.1103/PhysRevC.105.044905
54. X.L. Zhao, G.L. Ma, Search for the chiral magnetic effect in collisions between two isobars with deformed and neutron-rich nuclear structures. Phys. Rev. C **106**, 034909 (2022). https://doi.org/10.1103/PhysRevC.106.034909
55. F. Li, Y.G. Ma, S. Zhang, et al., Impact of nuclear structure on the background in the chiral magnetic effect in $^{96}_{44}$Ru + $^{96}_{44}$Ru and $^{96}_{40}$Zr + $^{96}_{40}$Zr collisions at $\sqrt{s_{NN}} = 7.7 \sim 200$ GeV from a multiphase transport model. Phys. Rev. C **106**, 014906 (2022). https://doi.org/10.1103/PhysRevC.106.014906
56. J. Jia et al., Imaging the initial condition of heavy-ion collisions and nuclear structure across the nuclide chart. Nucl. Sci. Tech. **35**, 220 (2024). https://doi.org/10.1007/s41365-024-01589-w
57. J.f. Wang, H.j. Xu, F.Q. Wang, Impact of initial fluctuations and nuclear deformations in isobar collisions. Nucl. Sci. Tech. **35**, 108 (2024). https://doi.org/10.1007/s41365-024-01480-8
58. Z. Yuan, A. Huang, W.H. Zhou et al., Evolution of topological charge through chiral anomaly transport. Phys. Rev. C **109**, L031903 (2024). https://doi.org/10.1103/PhysRevC.109.L031903
59. Z. Yuan, A. Huang, G. Xie, et al., Exploring the chiral magnetic effect in isobar collisions through Chiral Anomaly Transport. arXiv:2412.09130
60. H.j. Xu, J. Zhao, X. Wang, et al., Varying the chiral magnetic effect relative to flow in a single nucleus-nucleus collision. Chin. Phys. C **42**, 084103 (2018). https://doi.org/10.1088/1674-1137/42/8/084103
61. H.J. Xu, X. Wang, H. Li et al., Importance of isobar density distributions on the chiral magnetic effect search. Phys. Rev. Lett. **121**, 022301 (2018). https://doi.org/10.1103/PhysRevLett.121.022301
62. X.L. Zhao, G.L. Ma, Y.G. Ma, Impact of magnetic-field fluctuations on measurements of the chiral magnetic effect in collisions of isobaric nuclei. Phys. Rev. C **99**, 034903 (2019). https://doi.org/10.1103/PhysRevC.99.034903
63. S. Shi, Y. Jiang, E. Lilleskov et al., Anomalous chiral transport in heavy ion collisions from anomalous-viscous fluid dynamics. Annals Phys. **394**, 50–72 (2018). https://doi.org/10.1016/j.aop.2018.04.026
64. B.X. Chen, X.L. Zhao, G.L. Ma, Difference between signal and background of the chiral magnetic effect relative to spectator and participant planes in isobar collisions at sNN=200 GeV. Phys. Rev. C **109**, 024909 (2024). https://doi.org/10.1103/PhysRevC.109.024909
65. Z.W. Lin, C.M. Ko, B.A. Li et al., A Multi-phase transport model for relativistic heavy ion collisions. Phys. Rev. C **72**, 064901 (2005). https://doi.org/10.1103/PhysRevC.72.064901
66. G.L. Ma, Z.W. Lin, Predictions for $\sqrt{s_{NN}} = 5.02$ TeV Pb+Pb Collisions from a Multi-Phase Transport Model. Phys. Rev. C **93**, 054911 (2016). https://doi.org/10.1103/PhysRevC.93.054911
67. Z.W. Lin, L. Zheng, Further developments of a multi-phase transport model for relativistic nuclear collisions. Nucl. Sci. Tech. **32**, 113 (2021). https://doi.org/10.1007/s41365-021-00944-5
68. Z.W. Lin, Evolution of transverse flow and effective temperatures in the parton phase from a multi-phase transport model. Phys. Rev. C **90**, 014904 (2014). https://doi.org/10.1103/PhysRevC.90.014904
69. J.D. Orjuela Koop, A. Adare, D. McGlinchey, et al., Azimuthal anisotropy relative to the participant plane from a multiphase transport model in central p + Au , d + Au , and ^{3}He + Au collisions at $\sqrt{s_{NN}} = 200$ GeV. Phys. Rev. C **92**, 054903 (2015). https://doi.org/10.1103/PhysRevC.92.054903
70. G.L. Ma, A. Bzdak, Flow in small systems from parton scatterings. Nucl. Phys. A **956**, 745–748 (2016). https://doi.org/10.1016/j.nuclphysa.2016.01.057
71. Y. He, Z.W. Lin, Improved quark coalescence for a multi-phase transport model. Phys. Rev. C **96**, 014910 (2017). https://doi.org/10.1103/PhysRevC.96.014910
72. L. Huang, G.L. Ma, Study on higher moments of net-charge multiplicity distributions using a multiphase transport model. Chin. Phys. C **45**, 074110 (2021). https://doi.org/10.1088/1674-1137/abfd29
73. Q. Chen, G.L. Ma, Dynamical development of proton cumulants and correlation functions in Au+Au collisions at $\sqrt{s_{NN}} = 7.7$GeV from a multiphase transport model. Phys. Rev. C **106**, 014907 (2022). https://doi.org/10.1103/PhysRevC.106.014907
74. Q. Chen, H.S. Wang, G.L. Ma, Probing fluctuations and correlations of strangeness by net-kaon cumulants in Au+Au collisions at sNN=7.7 GeV. Phys. Rev. C **107**, 034910 (2023). https://doi.org/10.1103/PhysRevC.107.034910
75. G.L. Ma, B. Zhang, Effects of final state interactions on charge separation in relativistic heavy ion collisions. Phys. Lett. B **700**, 39–43 (2011). https://doi.org/10.1016/j.physletb.2011.04.057
76. A.M. Poskanzer, S.A. Voloshin, Methods for analyzing anisotropic flow in relativistic nuclear collisions. Phys. Rev. C **58**, 1671–1678 (1998). https://doi.org/10.1103/PhysRevC.58.1671
77. L.X. Han, G.L. Ma, Y.G. Ma et al., Initial fluctuation effect on harmonic flow in high-energy heavy-ion collisions. Phys. Rev. C **84**, 064907 (2011). https://doi.org/10.1103/PhysRevC.84.064907
78. L. Ma, G.L. Ma, Y.G. Ma, Parton collisional effect on the conversion of geometry eccentricities into momentum anisotropies in

relativistic heavy-ion collisions. Phys. Rev. C **103**, 014908 (2021). https://doi.org/10.1103/PhysRevC.103.014908
79. M. Nie, L. Yi, G. Ma et al., Influence of initial-state momentum anisotropy on the final-state collectivity in small collision systems. Phys. Rev. C **100**, 064905 (2019). https://doi.org/10.1103/PhysRevC.100.064905
80. M. Abdallah et al., Search for the chiral magnetic effect with isobar collisions at $\sqrt{s_{NN}}$=200 GeV by the STAR Collaboration at the BNL Relativistic Heavy Ion Collider. Phys. Rev. C **105**, 014901 (2022). https://doi.org/10.1103/PhysRevC.105.014901
81. J. Bloczynski, X.G. Huang, X. Zhang et al., Azimuthally fluctuating magnetic field and its impacts on observables in heavy-ion collisions. Phys. Lett. B **718**, 1529–1535 (2013). https://doi.org/10.1016/j.physletb.2012.12.030
82. S. Shi, H. Zhang, D. Hou et al., Signatures of chiral magnetic effect in the collisions of isobars. Phys. Rev. Lett. **125**, 242301 (2020). https://doi.org/10.1103/PhysRevLett.125.242301
83. L. Huang, M.W. Nie, G.L. Ma, Sensitivity analysis for observables of the chiral magnetic effect using a multiphase transport model. Phys. Rev. C **101**, 024916 (2020). https://doi.org/10.1103/PhysRevC.101.024916
84. G. Huang, J. Zhao, P. Zhuang, Quantum color screening in external magnetic field. Phys. Rev. D **107**, 114035 (2023). https://doi.org/10.1103/PhysRevD.107.114035